Electrostatically coupled tunable topological phononic metamaterials for angular velocity sensing

Jian Zhao [1,*] Xianze Zheng [1] Najib Kacem [2] Zeyuan Dong [1] and Pengbo Liu [1]

[1] *School of Automotive Engineering, State Key Laboratory of Structure Analysis for Industrial Equipment, Dalian University of Technology, Dalian 116081, China*

[2] *University of Franche-Comté, CNRS, FEMTO-ST Institute, Department of Applied Mechanics, F-25000 Besançon, France*

(Received 1 November 2023; revised 24 December 2023; accepted 2 January 2024; published 15 February 2024)

We propose an electrostatically coupled phononic metamaterial for angular velocity sensing, whose sensitivity is immune to external damping and local material defects; furthermore, the coupling strength and frequency range of bands are tunable by the voltages applied to the lattices. The induced Coriolis force could open up the topologically nontrivial band gaps, and the edge band bandwidths increase gradually with respect to the angular velocity. Hence, according to the dispersion relation of edge modes and the difference between edge states and bulk states, an angular velocity sensing method based on the band structure variation of the tunable phononic metamaterial is proposed by using the phase difference and amplitude ratio of edge states. In contrast to traditional amplitude-dependent microelectromechanical system gyroscopes, such a frequency-dependent angular velocity sensing method makes the sensitivity independent of the external damping coefficient. In addition, the topological properties ensure the robustness of the proposed angular velocity sensing method against local defects. The tunable metamaterial-based angular velocity sensing mechanism provides a bridge between physics and engineering applications.

DOI: 10.1103/PhysRevB.109.075136

I. INTRODUCTION

Metamaterials, as new artificial materials with novel properties, have attracted wide attention in recent years [1]. While conventional materials derive their mechanical and electrical characteristics from their attributed natural properties, metamaterials enable us to access new functionalities based on artificially designed unit structures. The road map of metamaterials applications has revealed the potential of metamaterials in sensing technology [2]. Due to the exotic properties of metamaterials, the interdisciplinary field between metamaterials science and sensing technology has become a new frontier [3], and considerable research for metamaterials-based sensors has been conducted in the fields of biosensing [4], thin-film sensing [5], wireless strain sensing [6], and inertial sensing [7]

In recent years, the theories of topological states in electronic systems, such as the quantum Hall effect (QHE) [8], quantum spin Hall effect [9], and topological insulators [10], have inspired the development of analogs in photonic [11,12], mechanical [13], and phononic metamaterials [14–20]. For the particular case of QHE, researchers have proposed several methods, including gyroscopic metamaterials [14,15], acoustic resonators with circulating airflow [16], and a rotating lattice with a Coriolis force [17], to break the time-reversal symmetry in phononic analogs and realize one-way edge states, which have the features of unidirectional propagation, confined to the boundary, robust to local defects and immune to backscattering.

Among these, particular attention is paid to a rotating lattice with a Coriolis force [17], which is a two-dimensional system formed by the periodic arrangement of springs and masses in a noninertial reference frame. The key to realizing the unique phenomenon of QHE in the classical system is by introducing the Coriolis force, which will break time-reversal symmetry and open up topologically nontrivial band gaps with one-way edge states. The intriguing phenomenon that the band structure varies with external angular velocity provides the possibility to design and manufacture a new angular velocity sensing system based on similar metamaterials. In addition, traditional microelectromechanical system (MEMS) gyroscopes, such as disk, bulk acoustic wave, quad mass, and wineglass gyroscopes [21], mainly adopt the amplitude signal as the output to sense angular velocity, however, this signal is susceptible to the external damping coefficient variation relating to air pressure [22,23]. In contrast to these typical amplitude-dependent MEMS gyroscopes, metamaterials whose band structure is sensitive to angular velocity open new degrees of freedom to design frequency-dependent gyroscopes.

Indeed, previous theoretical and experimental research on topological phononic metamaterials was mainly concerned with the intrinsic topological properties [14–20] and few studies have investigated the possibility of extending the metamaterials to the field of sensing [7]. In this paper, we designed a tunable phononic metamaterial (TPM) consisting of electrostatically coupled masses for angular velocity sensing. Compared with the existing phononic metamaterials with fixed coupling coefficients, electrostatic coupling provides convenience for its manufacture based on MEMS technology and high tunability for the coupling strength. When the TPM

*jzhao@dlut.edu.cn

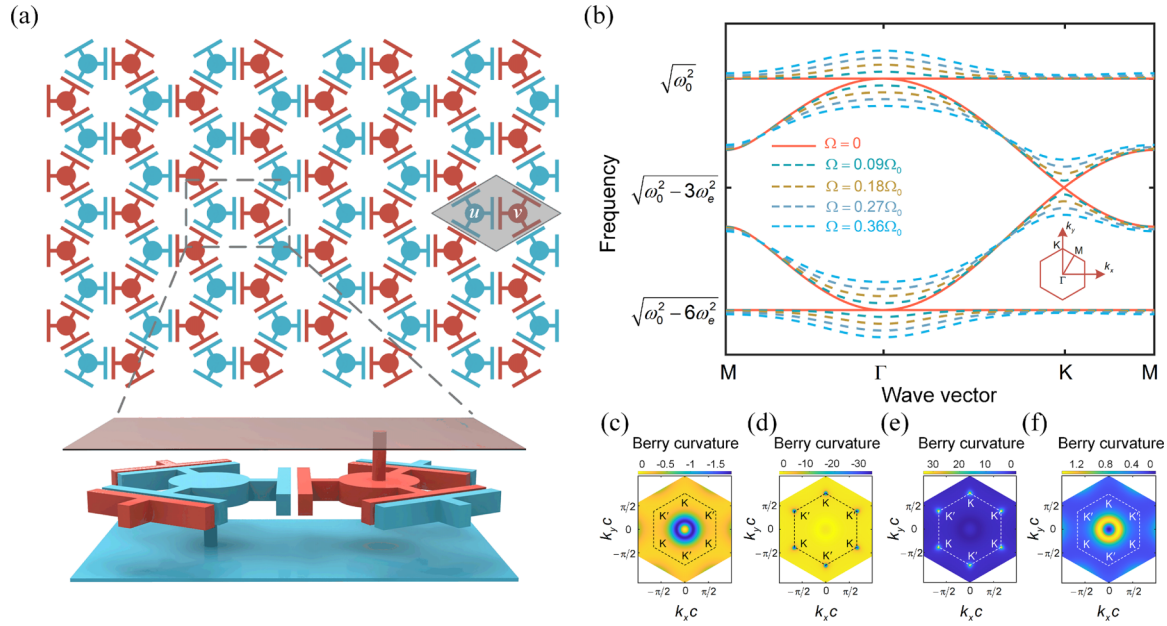

FIG. 1. (a) Schematic of the TPM. The dashed box shows the detailed structure of the lattice and the shadowed region is a unit cell of the lattice, where the blue and red parts correspond to the applied voltage of V_1 and V_2, respectively. (b) The band structures of TPM in the irreducible Brillouin zone with different angular velocities of $\Omega = 0$, $\Omega = 0.09\Omega_0$, $\Omega = 0.18\Omega_0$, $\Omega = 0.27\Omega_0$, and $\Omega = 0.36\Omega_0$. The inset is the Brillouin zone. (c)–(f) Berry curvatures of the first, second, third, and fourth bands, respectively, with an angular velocity of $\Omega = 0.09\Omega_0$.

is placed on a rotational framework, the introduction of the Coriolis force, as an external magneticlike bias, will open up topologically nontrivial band gaps. The band structure and topological properties of TPM are related to the value of angular velocity. According to the dispersion relation in the band gaps, we proposed a possible method using a phase-locked loop [24,25] to track the variation of band structure quickly and precisely. Based on that, a frequency-dependent angular velocity sensing system based on TPM is proposed and discussed in detail, which could offer different ideas and avenues for the design of angular velocity sensors.

II. THE BAND STRUCTURE FOR A TUNABLE PHONONIC METAMATERIAL

The TPM we propose here is constructed as a honeycomb lattice, as depicted in Fig. 1(a). Unlike a typical mass-spring crystal, adjacent lattice sites are coupled by the electrostatic force between capacitive plates. In each unit cell, which contains two masses M, one mass hangs from the roof plate and another one is supported by the substrate plate, as shown in the dashed box of Fig. 1(a). By applying different voltages V_1 and V_2 to the roof and substrate plates, electrostatic coupling $\varepsilon bl(V_1 - V_2)^2/2d_0^2$ is introduced between adjacent masses, where ε is the dielectric constant of the gap medium, b and l are the width and length of the electrode area, respectively, and d_0 is the original capacitor gap, which should be sufficiently small compared to l and much larger than the in-plane displacements of masses ψ. The cylinders connecting the masses to the roof or substrate plates play the role of restoring springs with a stiffness of k_0, preventing the occurrence of a pull-in phenomenon [26] under the working voltage. With the condition $\psi \ll d_0 \ll l$, linear components will dominate the dynamics of the metamaterials, while the electrostatic nonlinearity terms are negligible (detailed analyses of the linearized dynamic equations and the nonlinear effects are found in the Supplemental Material [27], with Refs. [17,26,28–32] therein). The linearized dynamic equations for a unit cell can be simplified to a frequency domain dynamic matrix [30],

$$\omega\begin{pmatrix}\psi\\ \dot{\psi}\end{pmatrix} = i\begin{pmatrix}0 & I\\ -D_k & \Gamma(\Omega)\end{pmatrix}\begin{pmatrix}\psi\\ \dot{\psi}\end{pmatrix}, \quad \psi = \begin{pmatrix}\psi_u\\ \psi_v\end{pmatrix}, \tag{1}$$

where I is the identity matrix, D_k is the positive-definite matrix containing restoring effects and electrostatic coupling terms, $\Gamma(\Omega)$ is the skew-symmetric matrix arising from Coriolis forces associated with angular velocity Ω as [33]

$$\begin{pmatrix}0 & 2\Omega & 0 & 0\\ -2\Omega & 0 & 0 & 0\\ 0 & 0 & 0 & 2\Omega\\ 0 & 0 & -2\Omega & 0\end{pmatrix}, \tag{2}$$

ψ is the in-plane displacement of mass u and v in a unit cell, and $(\psi \quad \dot{\psi})^T$ is the extended displacement-velocity vector. In order to solve Eq. (1) as a Hermitian eigenvalue problem, a suitable transformation [30,33],

$$T = \begin{pmatrix}\sqrt{D_k} & 0\\ 0 & i\end{pmatrix}, \tag{3}$$

can be applied to transform Eq. (1) into Hermitian form as

$$\omega\begin{pmatrix}\sqrt{D_k}\psi\\ i\dot{\psi}\end{pmatrix} = \begin{pmatrix}0 & \sqrt{D_k}\\ \sqrt{D_k} & i\Gamma(\Omega)\end{pmatrix}\begin{pmatrix}\sqrt{D_k}\psi\\ i\dot{\psi}\end{pmatrix}, \tag{4}$$

where $\sqrt{D_k}$ can be constructed by the positive eigenvalues and eigenvectors of D_k.

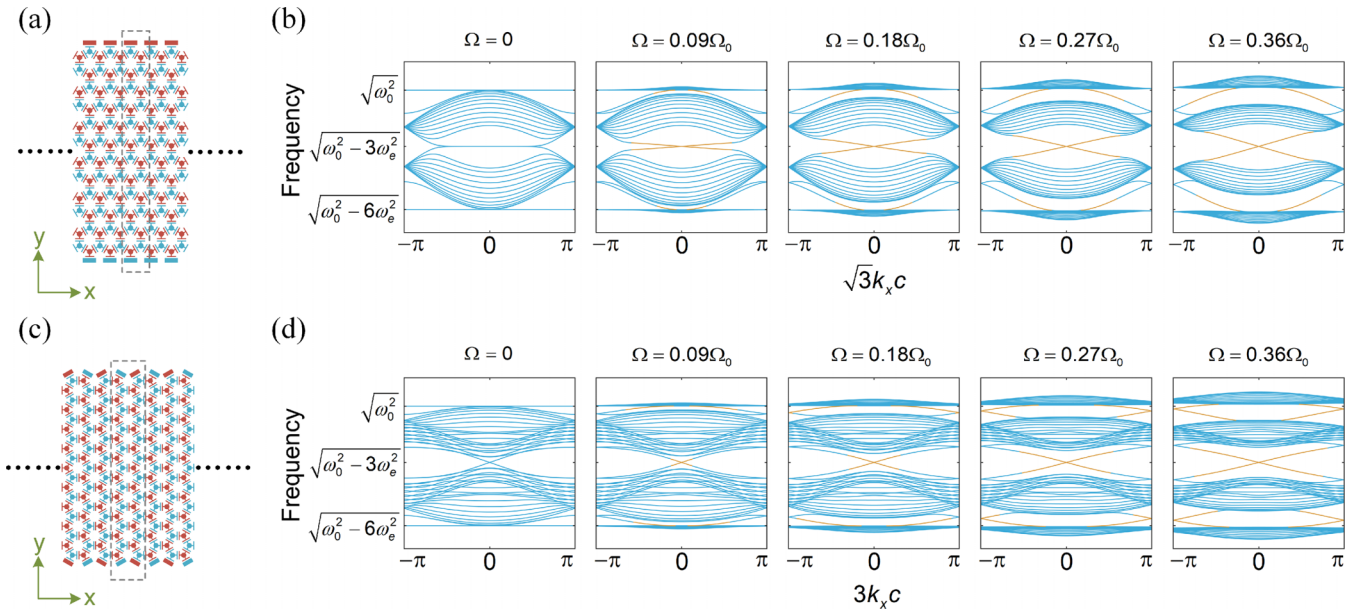

FIG. 2. Schematics of ribbon structures with (a) zigzag and (c) armchair boundaries, and the dashed boxes indicate the supercells for the two kinds of ribbon structures. The one-dimensional band structures for the supercells of (b) a zigzag boundary ribbon and (d) an armchair boundary ribbon with angular velocities of $\Omega = 0$, $\Omega = 0.09\Omega_0$, $\Omega = 0.18\Omega_0$, $\Omega = 0.27\Omega_0$, and $\Omega = 0.36\Omega_0$. Blue lines represent the bulk modes, and the yellow lines represent edge modes.

The band structures of TPM in the irreducible Brillouin zone with different angular velocities are shown in Fig. 1(b), where $\omega_0^2 = k_0/M$, $\omega_e^2 = \varepsilon b(V_1 - V_2)^2 l/2Md_0^3$, and for simplicity we set $\Omega_0 = \omega_e^2/\sqrt{\omega_0^2 - 3\omega_e^2}$. With the condition $\omega_0^2 \gg \omega_e^2$, which is necessary for the device to prevent the pull-in phenomenon [26], the band structure is almost symmetric with respect to frequency $\omega = \sqrt{\omega_0^2 - 3\omega_e^2}$, and the frequency range of the bands is tunable by adjusting the voltage $V_1 - V_2$. In the case of $\Omega = 0$, where time-reversal symmetry is preserved, the linear double degeneracy can be observed in the vicinity of the K point ($k_x = 0 \quad k_y = 4\pi/3\sqrt{3}c$), where c is the distance between adjacent lattice sites. The introduction of angular velocity $\Omega < 3\omega_e^2/4\sqrt{\omega_0^2 - 3\omega_e^2} = 0.75\Omega_0$ will break time-reversal symmetry and open three band gaps by lifting the degeneracies of the four bands. As the angular velocity increases, the band gaps are gradually widened (the angular velocity range considered in this paper is mainly to ensure the linearity and consistency of the bandwidth variation trend; an investigation for the case of larger angular velocity can be found in Ref. [17]).

The topological nature of the bands is characterized by the Chern numbers, which can be obtained by integrating Berry curvature over the entire first Brillouin zone. For the case with nonzero angular velocity, the Berry curvatures for all four bands are shown in Figs. 1(c)–1(f), and the corresponding Chern numbers are calculated as $\{-1, 0, 0, 1\}$ (the calculations of Berry curvatures and Chern numbers are detailed in the Supplemental Material [27], with Refs. [14,34–37] therein). The sum of Chern numbers below the band gaps is nonzero, which means that the band gaps are topologically nontrivial and indicates the existence of gapless one-way edge states in the band gaps. Thus, these bulk band gaps can be labeled as edge bands. To further investigate the dispersion relation of edge modes and effects of angular velocity in detail, two kinds of ribbon structures with zigzag and armchair boundaries in the y direction, respectively, and infinite length in the x direction are considered, as shown in Figs. 2(a) and 2(c). The band structures for the supercells of the ribbons show that there are two edge modes, corresponding to the modes confined to the top and bottom boundaries, within the frequency range of each edge band, as illustrated in Figs. 2(b) and 2(d). In agreement with the analysis of the band structure in the Brillouin zone, the bandwidths of the edge bands increase gradually with respect to the angular velocity. In addition, it is worth noting that a variation of the angular velocity will change the slopes of the edge mode dispersion curves (group velocity), but will not affect the intersection point of the dispersion curves in the second edge band with the line $k_x = 0$, which is fixed at ($0 \quad \sqrt{\omega_0^2 - 3\omega_e^2}$). These effects of angular velocity on the band structure form the basis for the potential application of TPM in the angular velocity sensing field.

III. ANGULAR VELOCITY SENSING METHOD

To verify the difference between the edge states and bulk states and then further promote the TPM for angular velocity sensing by this difference, numerical simulations of a finite TPM system consisting of 43×12 unit cells are performed. This TPM system has both zigzag and armchair boundaries and can be excited by the driving electrodes symmetrically placed on the left and right boundaries. In the case of $\Omega = 0.36\Omega_0$, by applying a combination of coupling voltage (V_1 or V_2) and small harmonic voltage $V_{ac}\cos(\omega t)$,

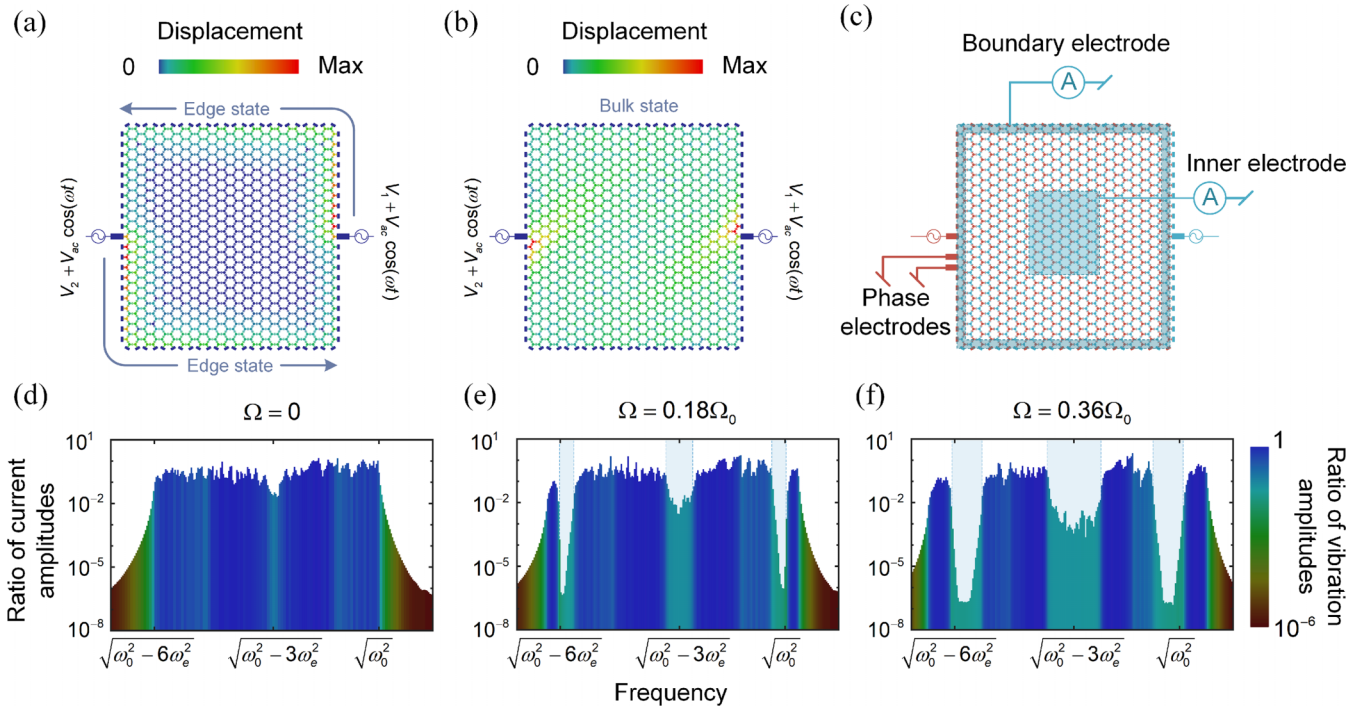

FIG. 3. (a) Numerical simulation for the edge state of a finite TPM system. Only the masses near the boundary would vibrate. (b) Numerical simulation for the bulk state of the system. Both inner and boundary masses vibrate. (c) The arrangement of the boundary electrode, inner electrode, and phase electrodes. Numerical simulations for the ratios of current amplitudes for the inner electrode to the boundary electrode with angular velocities of (d) $\Omega = 0$, (e) $\Omega = 0.18\Omega_0$, and (f) $\Omega = 0.36\Omega_0$ at the frequencies over all bands. The light blue shaded regions bounded by dashed lines correspond to the theoretical calculation results of edge band bandwidths.

$V_{ac} \ll |V_1 - V_2|$ to the driving electrodes, the edge state ($\omega = \sqrt{\omega_0^2 - 3\omega_e^2}$) and bulk state ($\omega = \sqrt{\omega_0^2 - 3\omega_e^2/2}$) can be excited, respectively, as shown in Figs. 3(a) and 3(b).

It can be clearly seen that the mechanical wave of the edge state propagates along the boundary unidirectionally so that only the masses near the boundary would vibrate (Supplemental Movie 1 [27]), while the bulk state can scatter into the bulk of the system, causing both inner and boundary masses to vibrate (Supplemental Movie 2 [27]). Such a significant difference in mechanical wave propagation characteristics indicates that the edge state and bulk state can be distinguished by detecting the vibrations of the inner and boundary masses of the TPM system. Thus, we can divide the inner and boundary detection electrodes from the roof plate, as shown in Fig. 3(c). The vibration of inner and boundary masses will cause variations of relevant capacitances and generate the currents on the inner and boundary electrodes. By detecting the ratio of current amplitudes on the two electrodes ($I_{\text{in}}/I_{\text{bo}}$) at the frequencies over all bands, the frequency ranges of the edge states can be measured. Then, the value of angular velocity, which is related to the bandwidths of the edge bands, can be sensed accurately. Figures 3(d)–3(f) show the ratios of current amplitudes for the inner electrode to the boundary electrode. The current amplitude ratio decreases significantly in the frequency range of the edge bands, which can be used to confirm the bandwidths of the edge bands. Moreover, the change of edge band bandwidth with angular velocity is in good agreement with the results of the theoretical calculation, as shown in the light blue shaded regions of Figs. 3(e) and 3(f). Furthermore, from a practical perspective, the direct frequency sweeping over the range of all bands is time consuming and the accuracy will be limited by the sweep step. Therefore, the phase-locked loop [24,25], which is commonly used in frequency-dependent sensors [38,39], can be adopted to track the variation of edge bands quickly and accurately. According to the dispersion relation of edge modes in Fig. 2, particularly in the second edge band, the dispersion curves are nearly straight lines, and the absolute values of the dispersion curve slopes (group velocity) increase with the angular velocity. By detecting the change of phase difference between adjacent supercells $\sqrt{3}k_{x1}c - \sqrt{3}k_{x2}c$ at two close excitation frequencies ω_1 and ω_2 in the second edge band, this slope can be obtained in the form of slope $= (\omega_1 - \omega_2)/(\sqrt{3}k_{x1}c - \sqrt{3}k_{x2}c)$. The intersection points of dispersion curves with $k_x = 0$ are fixed at $(0 \quad \sqrt{\omega_0^2 - 3\omega_e^2})$, and with the bulk bands are $(\pm\pi/3 \quad \omega_{u/l})$, where ω_u and ω_l are the upper and lower boundaries of the second edge band, respectively. Thus, the second edge band bandwidth $\omega_u - \omega_l$ can be derived as

$$\omega_u - \omega_l = \left| \frac{2\pi}{3\sqrt{3}} \frac{\omega_1 - \omega_2}{k_{x1}c - k_{x2}c} \right|. \tag{5}$$

Regarding the realization of edge band bandwidth variation tracking, which is caused by angular velocity, two additional phase electrodes are arranged in the TPM system to detect the phase difference between adjacent lattices located at the boundary, as shown in Fig. 3(c). The phase differences of the current signals on the two phase electrodes at the excitation

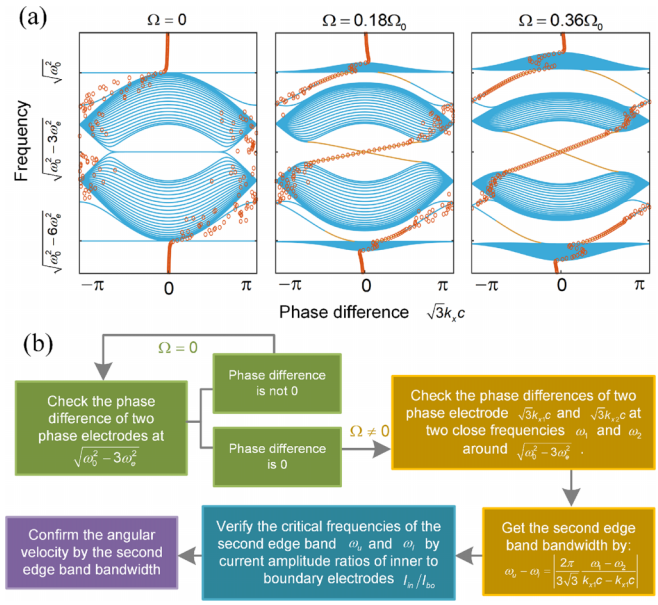

FIG. 4. (a) The phase differences of current signals on the two phase electrodes at the frequencies over all bands (orange circles) and the one-dimensional band structures for the supercells of the zigzag boundary ribbon (blue and yellow lines) with angular velocities of $\Omega = 0$, $\Omega = 0.18\Omega_0$, and $\Omega = 0.36\Omega_0$. (b) The workflow for the TPM-based angular velocity sensing method.

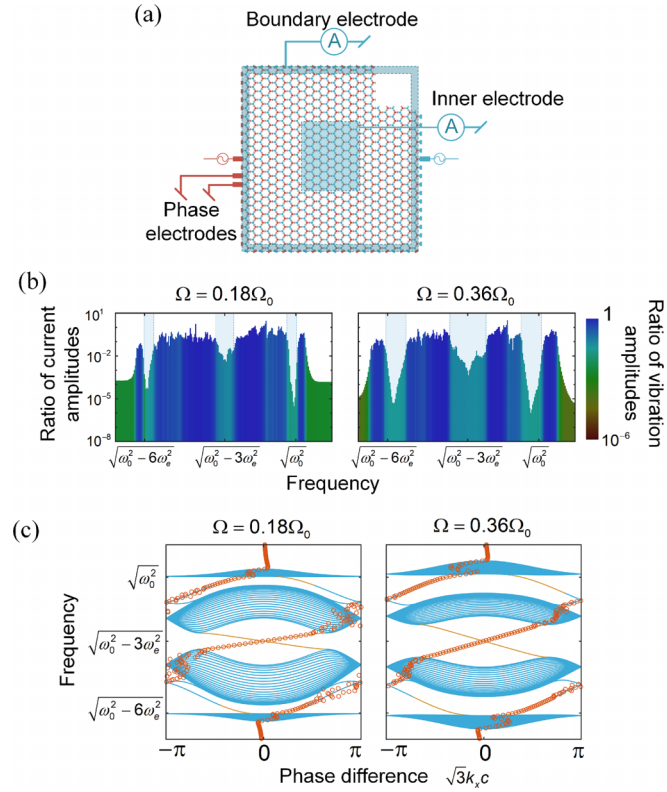

FIG. 5. (a) The defective TPM-based angular velocity sensing system, whose upper right part is missing. (b) Numerical simulations for the ratios of current amplitudes for the defective system with angular velocities of $\Omega = 0.18\Omega_0$ and $\Omega = 0.36\Omega_0$ at the frequencies over all bands. (c) The phase differences of current signals on the two phase electrodes for the defective system with angular velocities of $\Omega = 0.18\Omega_0$ and $\Omega = 0.36\Omega_0$ at the frequencies over all bands.

frequencies over all bands are shown in Fig. 4(a). It can be seen that the variation of phase difference with frequency is in good agreement with the dispersion relation in the edge bands. However, due to the coupling of multiple bulk modes, there is no obvious rule for the variation of the phase difference in bulk bands. Therefore, based on the above analysis, the workflow for the angular velocity sensing method is presented in Fig. 4(b), which combines the current amplitude ratios and the dispersion relations of edge modes in the second edge band to detect angular velocity, ensuring the accuracy and speed of detection.

The sensitivity of the proposed TPM-based angular velocity sensing method can be approximately expressed as

$$\frac{\omega_u - \omega_l}{\Omega} = \frac{\sqrt{\omega_0^2 - 3\omega_e^2/2} - \sqrt{\omega_0^2 - 9\omega_e^2/2}}{3\omega_e^2 \Big/ 4\sqrt{\omega_0^2 - 3\omega_e^2}}, \tag{6}$$

which only depends on the restoring term ω_0^2 and electrostatic coupling term ω_e^2, and is independent of the external damping coefficient. This feature enables the proposed TPM-based angular velocity sensing method to eliminate the need for vacuum packaging, which facilitates its fabrication and long-term storage.

Moreover, the inherent robustness against local defects is one of the most conspicuous characteristics of the TPM-based angular velocity sensing method. Numerical simulations are performed for a defective TPM system, whose upper right part is missing, as shown in Fig. 5(a). With angular velocities of $\Omega = 0.18\Omega_0$ and $\Omega = 0.36\Omega_0$, the ratios of current amplitudes for the inner electrode to boundary electrode and the phase differences of the current signals on the two phase electrodes are shown in Figs. 5(b) and 5(c), respectively. What can be clearly seen is that the results for the bandwidth variation of edge bands and the variation of the phase difference with frequency remain unchanged, which proves that the performance of this sensing method is not susceptible to local defects.

IV. CONCLUSION

In summary, a tunable phononic metamaterial consisting of electrostatically coupled masses is designed for angular velocity sensing. The linearized motion equations of the TPM subjected to angular velocity are derived. Based on the analysis of the band structure, the topologically nontrivial nature of the TPM system is verified, and the edge band bandwidths increase gradually with the increase of angular velocity. According to the significant difference between edge states and bulk states in mechanical wave propagation characteristics, an approach by detecting the current amplitude ratio of inner electrode to boundary electrode is proposed to confirm the edge band bandwidth variation due to angular velocity. Furthermore, to improve the speed and accuracy of detection, the phase-locked loop can be adopted to track the variation of the second edge band bandwidth based on the dispersion

relations of the edge modes. A comparison of the TPM-based angular velocity sensing method with traditional amplitude-dependent gyroscopes shows that the proposed method is independent of the external damping coefficient. Moreover, the robustness against the local defects for the TPM-based angular velocity sensing method is numerically verified. This frequency-dependent angular velocity sensing method based on TPM provides a feasible scheme for the design of MEMS gyroscopes robust to external damping coefficients and local defects.

ACKNOWLEDGMENTS

We gratefully acknowledge financial support by National Natural Science Foundation of China (Grant No. U1930206), and EUR EIPHI program, Europe (Contract No. ANR 17-EURE-0002).

[1] H. Huang, J. Chen, and S. Huo, Recent advances in topological elastic metamaterials, J. Phys.: Condens. Matter **33**, 503002 (2021).

[2] N. I. Zheludev, The road ahead for metamaterials, Science **328**, 582 (2010).

[3] T. Chen, S. Li, and H. Sun, Metamaterials application in sensing, Sensors **12**, 2742 (2012).

[4] H.-J. Lee and J.-G. York, Biosensing using split-ring resonators at microwave regime, Appl. Phys. Lett. **92**, 254103 (2008).

[5] I. A. I. Al-Naib, C. Jansen, and M. Koch, Thin-film sensing with planar asymmetric metamaterial resonators, Appl. Phys. Lett. **93**, 083507 (2008).

[6] R. Melik, E. Unal, N. K. Perkgoz, C. Puttlitz, and H. V. Demir, Metamaterial based telemetric strain sensing in different materials, Opt. Express **18**, 5000 (2010).

[7] X. Zheng, J. Zhao, N. Kacem, and P. Liu, Toward acceleration sensing based on topological gyroscopic metamaterials, Phys. Rev. B **106**, 094307 (2022).

[8] K. V. Klitzing, The quantized Hall effect, Rev. Mod. Phys. **58**, 519 (1986).

[9] B. A. Bernevig, T. L. Hughes, and S.-C. Zhang, Quantum spin Hall effect and topological phase transition in HgTe quantum wells, Science **314**, 1757 (2006).

[10] M. Z. Hasan and C. L. Kane, *Colloquium*: Topological insulators, Rev. Mod. Phys. **82**, 3045 (2010).

[11] F. D. M. Haldane and S. Raghu, Possible realization of directional optical waveguides in photonic crystals with broken time-reversal symmetry, Phys. Rev. Lett. **100**, 013904 (2008).

[12] Z. Wang, Y. D. Chong, J. D. Joannopoulos, and M. Soljačić, Reflection-free one-way edge modes in a gyromagnetic photonic crystal, Phys. Rev. Lett. **100**, 013905 (2008).

[13] C. L. Kane and T. C. Lubensky, Topological boundary modes in isostatic lattices, Nat. Phys. **10**, 39 (2014).

[14] P. Wang, L. Lu, and K. Bertoldi, Topological phononic crystals with one-way elastic edge waves, Phys. Rev. Lett. **115**, 104302 (2015).

[15] L. M. Nash, D. Kleckner, A. Read, V. Vitelli, A. M. Turner, and W. T. M. Irvine, Topological mechanics of gyroscopic metamaterials, Proc. Natl. Acad. Sci. USA **112**, 14495 (2015).

[16] A. B. Khanikaev, R. Fleury, S. H. Mousavi, and A. Alu, Topologically robust sound propagation in an angular-momentum-biased graphene-like resonator lattice, Nat. Commun. **6**, 8260 (2015).

[17] Y.-T. Wang, P.-G. Luan, and S. Zhang, Coriolis force induced topological order for classical mechanical vibrations, New J. Phys. **17**, 073031 (2015).

[18] E. Prodan and C. Prodan, Topological phonon modes and their role in dynamic instability of microtubules, Phys. Rev. Lett. **103**, 248101 (2009).

[19] J. Lu, C. Qiu, L. Ye, X. Fan, M. Ke, Fan. Zhang, and Z. Liu, Observation of topological valley transport of sound in sonic crystals, Nat. Phys. **13**, 369 (2017).

[20] R. Süsstrunk and S. D. Huber, Observation of phononic helical edge states in a mechanical topological insulator, Science **349**, 47 (2015).

[21] Q. Li, D. Xiao, X. Zhou, Y. Xu, M. Zhou, Z. Hou, K. He, Y. Zhang, and X. Wu, 0.04 degree-per-hour MEMS disk resonator gyroscope with high-quality factor (510 k) and long decaying time constant (74.9 s), Microsyst. Nanoeng. **4**, 32 (2018).

[22] Y. Wang, Y.-W. Lin, J. Glaze, G. D. Vukasin, D. D. Shin, H.-K. Kwon, D. B. Heinz, Y. Chen, D. D. Gerrard, T. W. Kenny, and A. M. Shkel, Quantification of energy dissipation mechanisms in toroidal ring gyroscope, J. Microelectromech. Syst. **30**, 193 (2021).

[23] X. Zhou, D. Xiao, Z. Hou, Q. Li, Y. Wu, and X. Wu, Influences of the structure parameters on sensitivity and Brownian noise of the disk resonator gyroscope, J. Microelectromech. Syst. **26**, 519 (2017).

[24] G.-C. Hsieh and J. C. Hung, Phase-locked loop techniques. A survey, IEEE Trans. Ind. Electron. **43**, 609 (1996).

[25] D. Abramovitch, Phase-locked loops: A control centric tutorial, in *Proceedings of the 2002 American Control Conference* (IEEE, New York, 2002), Vol. 1, pp. 1–15.

[26] M. I. Younis, *MEMS Linear and Nonlinear Static and Dynamics* (Springer, Berlin, 2011).

[27] See Supplemental Material at http://link.aps.org/supplemental/10.1103/PhysRevB.109.075136 for the linearized dynamic equations for a unit cell, the effects of electrostatic nonlinear terms, and the calculations of Berry curvatures and Chern numbers, which includes Refs. [28,29,31,32,34–37].

[28] M. I. Ibrahim and M. I. Younis, Enhancing the sensitivity of a resonant accelerometer, in *ASME 2008 International Mechanical Engineering Congress and Exposition* (ASME, New York, 2008), Vol. 11, pp. 241–247.

[29] J. Zhu, C. Q. Ru, and A. Mioduchowski, High-order subharmonic parametric resonance of multiple nonlinearly coupled micromechanical nonlinear oscillators, Acta. Mech. **212**, 69 (2010).

[30] R. Süsstrunk and S. D. Huber, Classification of topological phonons in linear mechanical metamaterials, Proc. Natl. Acad. Sci. USA **113**, E4767 (2016).

[31] A. H. Nayfeh, *Perturbation Methods* (Wiley-VCH, Weinheim, Germany, 2000).

[32] A. H. Nayfeh and D. T. Mook, *Nonlinear Oscillations* (Wiley, New York, 1995).

[33] Y. Liu, Y. Xu, S.-C. Zhang, and W. Duan, Model for topological phononics and phonon diode, Phys. Rev. B **96**, 064106 (2017).

[34] Y. Ando, Topological insulator materials, J. Phys. Soc. Jpn. **82**, 102001 (2013).

[35] D. Xiao, M.-C. Chang, and Q. Niu, Berry phase effects on electronic properties, Rev. Mod. Phys. **82**, 1959 (2010).

[36] H. Wang, X. Tang, H. Xu, J. Li, and X. Qian, Generalized Wilson loop method for nonlinear light-matter interaction, NPJ Quantum Mater **7**, 61 (2022).

[37] T. Fukui, Y. Hatsugai, and H. Suzuki, Chern numbers in discretized Brillouin zone: Efficient method of computing (spin) Hall conductances, J. Phys. Soc. Jpn. **74**, 1674 (2005).

[38] A. Demir and M. S. Hanay, Fundamental sensitivity limitations of nanomechanical resonant sensors due to thermomechanical noise, IEEE Sens. J. **20**, 1947 (2019).

[39] T. Hiller, Z. Pentek, J.-T. Liewald, A. Buhmann, and H. Roth, Origins and mechanisms of bias instability noise in a three-axis mode-matched MEMS gyroscope, J. Microelectromech. Syst. **28**, 586 (2019).